UC Berkeley
UC Berkeley Previously Published Works

Title

Observing atmospheric clouds through stereo reconstruction

Permalink

https://escholarship.org/uc/item/7cx3m61s

Authors

Öktem, Ruşen
Romps, David M

Publication Date

2015-03-17

DOI

10.1117/12.2083395

Peer reviewed

eScholarship.org Powered by the California Digital Library
University of California

atmospheric clouds through stereo reconstruction

Ruşen Öktem; David M. Romps
Author Affiliations +

Proceedings Volume 9393, Three-Dimensional Image Processing, Measurement (3DIPM), and Applications 2015; 93930H (2015) https://doi.org/10.1117/12.2083395
Event: SPIE/IS&T Electronic Imaging, 2015, San Francisco, California, United States

- ARTICLE
- SECTIONS
- FIGURES & TABLES
- SUPPLEMENTAL CONTENT
- REFERENCES
- CITED BY

Abstract

Observing cloud lifecycles and obtaining measurements on cloud features are significant problems in atmospheric cloud research. Scanning radars have been the most capable instruments to provide such measurements, but they have shortcomings when it comes to spatial and temporal resolution. High spatial and temporal resolution is particularly important to capture the variations in developing convections. Stereo photogrammetry can complement scanning radars with the potential to observe clouds as distant as tens of kilometers and to provide high temporal and spatial resolution, although it comes with the calibration challenges peculiar to various outdoor settings required to collect measurements on atmospheric clouds. This work explores the use of stereo photogrammetry in atmospheric cloud research, focusing on tracking vertical motion in developing convections. Calibration challenges and strategies to overcome these challenges are addressed within two different stereo settings in Miami, Florida and in the plains of Oklahoma. A feature extraction and matching algorithm is developed and implemented to identify cloud features of interest. A two-level resolution hierarchy is exploited in feature extraction and matching. 3D positions of cloud features are reconstructed from matched pixel pairs, and cloud tops of developing turrets in shallow to deep convection are tracked in time to estimate vertical accelerations. Results show that stereophotogrammetry provides a useful tool to observe cloud lifecycles and track the vertical acceleration of turrets exceeding 10 km height.

1. INTRODUCTION

Atmospheric clouds play an important role in regulating earth’s climate and hydrological cycle. Understanding cloud dynamics is a significant problem in atmospheric research and it requires observing lifecycles and obtaining measurements on the clouds such as the motion and growth rate of convections. Various instruments such as lidars, ceilometers and millimeter wavelength radars are used for meteorological measurements. Among these instruments, millimeter wavelength radars have the capability to measure the condensates and motions within clouds but capturing the lifecycle of clouds require a scanning radar. W-band scanning radars at the Atmospheric Radiation Measurement (ARM) sites employ different scanning strategies for collecting precipitation and cloud characteristics.[1, 2] For example, the Boundary-Layer Range-Height-Indicator (BL-RHI) scan strategy covers 90° of elevation (horizon to zenith) and 80° of azimuth to map the sky with a resolution of 1 degree in elevation and 2 degrees in azimuth once every 5 minutes.[3, 4] This will image a convective cloud at a distance 20 km rising at 10 m/s with a transverse resolution of 700 meters and a vertical displacement of the cloud between scans of 3 km. This resolution is not high enough to capture lifecycle of clouds rising at around 10 m/s or higher, whereas a consumer camera with a modest 0.1-Hz frame rate will image the cloud with a resolution of about a few tens of meters and a vertical displacement between images of 100 meters. With this spatial and temporal resolution, stereo photogrammetry can provide detailed cloud-lifecycle data and complement radars.

Early use of stereo photogrammetry in atmospheric research in 1950s relied on analog photographs to obtain cloud positions and velocities.[5-8] More recently, digital camera pairs have been used,[9–12] for obtaining similar measurements, which opens up the possibility of using digital image processing algorithms to automate the cloud detection[13] or feature detection and reconstruction process.[14] In all stereo reconstruction studies, the essential first step is the careful calibration of camera positions and orientations. Orientation of the cameras i.e., the determination of the camera's three Euler angles is often the trickiest step. Previous approaches have used the positions of known landmarks, such as topographic features[15] or the positions of stars.[14] In this study, we introduce the calibration challenges in two different outdoor settings with long baseline, and present strategies to overcome them. Next, we describe a feature detection and matching algorithm to detect cloud features from a pair of stereo images and reconstruct their 3D locations. We present the calibration and automatic recognition performance over different types of clouds captured at two different locations where atmospheric data are collected.

2.

OBSERVATION SYSTEM SETUP

This paper presents two different settings in Miami, Florida, USA and at the Southern Great Plains (SGP) ARM site in Oklahoma, USA (see Fig. 1). The two cameras of Miami setting captures ocanic clouds off the coast, where they overlook Biscayne Bay (25.6° N, 80.2° W). One of the cameras (a 5-megapixel Stardot NetCam SC) is mounted on the roof of the Marine and Science Technology (MAST) Academy. This camera will be referred as the right camera throughout the text. The left camera (a 3-megapixel Stardot NetCam XL) is mounted on the roof of the Rosenstiel School of Marine and Atmospheric Science (RSMAS) as part of South Florida's Cloud-Aerosol-Rain Observatory* (CAROb). It is located 296 m to the east and 822 m to the south of the right camera. The right and left cameras face 6.56° and 18.19° west of south, and they capture still images at 1296×960 and 1024×768 pixel resolution in lossy jpeg format with a field of view of 67° and 76°, respectively. The two cameras are connected to separate servers, and so are controlled independently from each other, but they are synchronized to a common time server. Both cameras have 1/2" 4-8 mm varifocal lenses set at wide angle for a wider field of view. The right camera of the SGP setting is mounted on a tower at 36.7° N, 97.5° W GPS location. The left camera is located 720 m to the south and 138 m to the east of the right camera, mounted on a pole attached to a trailer. The two IQeye Sentinel Series H.264 5-MP indoor/outdoor cameras have 1/2" 4-8 mm varifocal lenses set at wide angle. The left camera is 721m to the south and 138m to the west of the right camera. The right and left cameras face 8.81° and 4.88° south of west, and have 76° and 86° field of views, respectively. The two cameras of the SGP setting are connected to the same single server and hence controlled by the same single firmware to capture and store still images at 2592x1944 pixel resolution in lossy jpeg format. The terrain of the SGP site is at around 310 m elevation from the sea level.

Figure 1.

The locations of Miami (top) and SGP (bottom) settings, shown as three maps with increasing zoom from left to right. The red squares in the left and middle panels indicate the regions displayed in the middle and right panels, respectively. The red rectangles in the right panel indicate the locations of the two cameras.

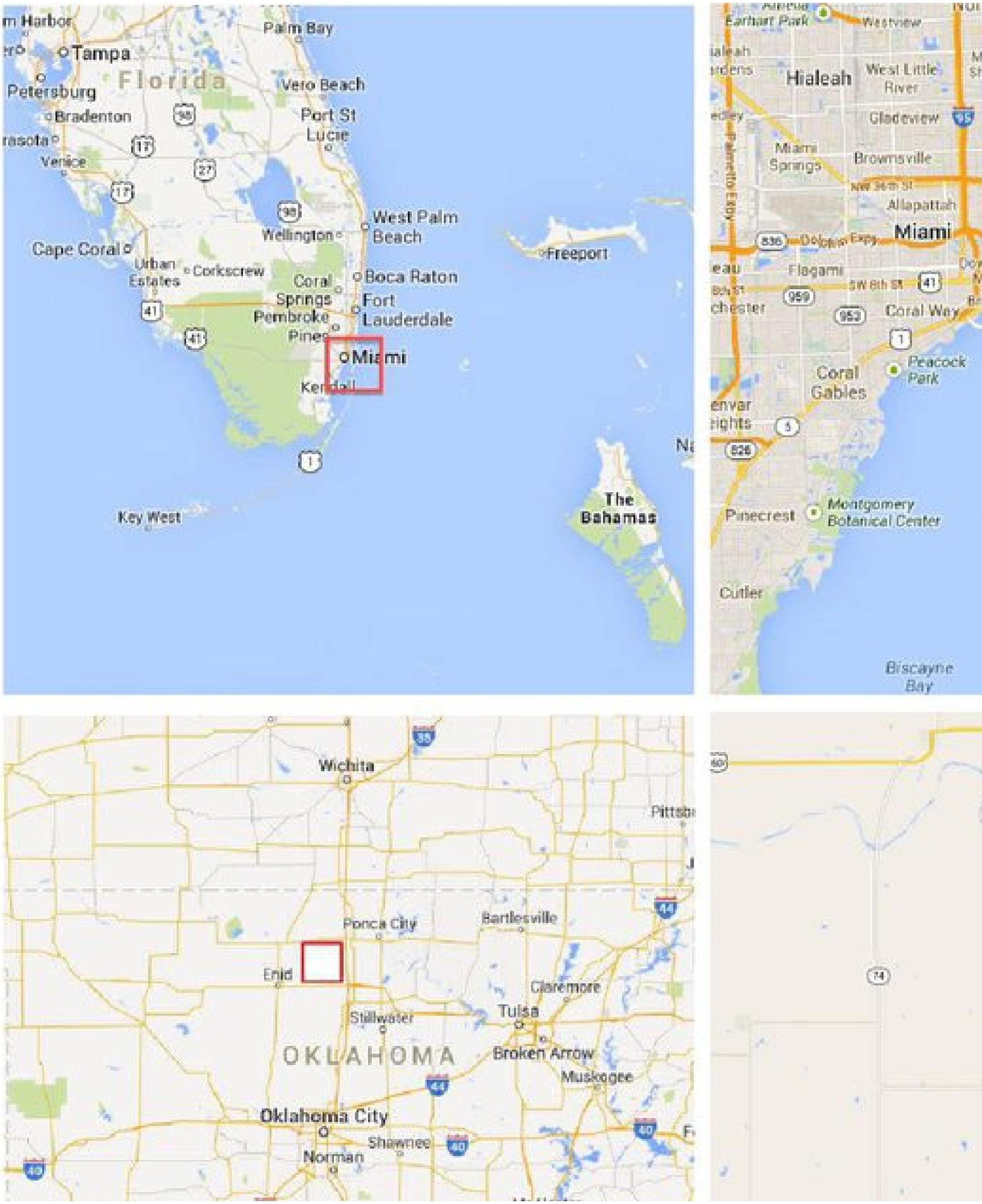
Tampa
Florida
Petersburg
Bradenton
Venice
Palm Bay
Vero Beach
Port St Lucie
West Palm Beach
Wellington
Cape Coral
Urban Estates
Corkscrew
Coral Springs
Boca Raton
Fort Lauderdale
Pembroke Pines
Miami
Kendall
Freeport
Key West
The Bahamas
Earhart Park
Westview
Hialeah
West Little River
Gladeview
Miami Springs
Brownsville
Allapattah
Miami
Flagami
Coral Way
Coral Gables
Peacock Park
Pinecrest
Montgomery Botanical Center
Cutler
Biscayne Bay
Wichita
Ponca City
Bartlesville
Enid
Claremore
Stillwater
Tulsa
Broken Arrow
OKLAHOMA
Muskogee
Oklahoma City
Shawnee
Norman

3.

CALIBRATION STRATEGIES

Before introducing the two calibration strategies, let us briefly review the 3D projection equations associated with the pinhole camera model. Let **X** = (x, y, z, 1) denote the homogenous coordinates of a point in 3D space. Similarly, let **X′** = (x', y', 1) be the homogeneous coordinates of the image in the image plane. The relation between **X** and **X′** is expressed as[16]

$$\mathbf{X}' = \mathbf{P}\mathbf{X},$$

where projection matrix **P** is the product of the camera matrix **C**, rotation matrix **R**, and translation matrix **T**,

$$\mathbf{P} = \mathbf{C}\mathbf{R}\mathbf{T}.$$

The camera matrix **C** is composed of the focal length f in mm, density of pixels k_x (k_y) (i.e., number of pixels per distance, in the image plane's x' (y') direction), and principal point coordinate of the image plane c_x (c_y) as

$$\mathbf{C} = \begin{bmatrix} fk_x & 0 & c_x \\ 0 & fk_y & c_y \\ 0 & 0 & 1 \end{bmatrix}.$$

The rotation matrix **R** aligns the world coordinates (x,y,z) into the coordinate system aligned with the camera. Letting θ_1, θ_2, and θ_3 denote the three Euler angles of pitch, yaw, and roll, and x_0, y_0, and z_0 denote the camera's world coordinates, **R** and **T** can be expressed as

$$\mathbf{R} = \begin{bmatrix} 1 & 0 & 0 \\ 0 & \cos\theta_1 & \sin\theta_1 \\ 0 & -\sin\theta_1 & \cos\theta_1 \end{bmatrix} \begin{bmatrix} \cos\theta_2 & 0 & -\mathrm{s} \\ 0 & 1 & \\ \sin\theta_2 & 0 & \mathrm{c} \end{bmatrix}$$

If the projection matrices for a stereo pair of cameras can be constructed by the above equations, the 3D world position of a point in space can be reconstructed from the projection of the point in two camera image planes via direct linear transformation (DLT) method.[17] The estimation of camera matrix parameters is called intrinsic camera calibration and is often a straightforward problem that can be solved by calibration packages such as OpenCv libraries,.[18] OpenCv camera calibration library can also be used to estimate lens distortion correction parameters. Wide angle lenses used in our all four cameras cause noticeable radial distortion that cannot be ignored as in previous works.[11, 13, 15]

The parameters of the rotation and translation matrices are called the extrinsic parameters and should be estimated after the cameras are mounted in place. Uncontrollable environment of outdoor settings with a long baseline makes this step the most challenging part of the calibration process. It is possible to obtain the translation matrix parameters by GPS positioning but estimation of Euler angles often relies on at least three external landmarks of known 3D world coordinates. However, outdoor settings may lack reliable landmarks depending on the geography. We propose two different approaches for such cases, one exploiting the ocean horizon together with the epipolar constraint for the oceanic Miami setting and the other exploiting stars whenever night time image capturing is possible.

3.1

Using the Horizon in Extrinsic Camera Calibration

The horizon is the set of world coordinates where lines emanating from the camera touch the Earth's surface as a tangent. Consider a setup where horizon over the ocean is visible in the camera field of view and let the earth radius, horizontal displacement of the horizon from the camera, and the vertical displacement of the horizon from the sea level be denoted by dH and $\tilde{h}$, respectively. Assuming that the Earth is a sphere and the camera height from the sea level is much smaller than the Earth radius,

$$d_H = \sqrt{2R_e h},\ \tilde{h} = h.$$

can be derived[19] where R_e and h denote the radius of the Earth and camera height from the sea level, respectively. Then, the horizon for a camera positioned at (x_r, y_r, h_r) can be described by the set of 3D points

$$\left\{x_{H_r}, y_{H_r}, z_{H_r} \mid (x_{H_r} - x_r)^2 + (y_{H_r} - y_r)^2 = 2R\right.$$

and the projection of the horizon can be assumed as a line in the camera's image plane, which can be described by the set of pixels

$$\left\{x'_{H_r}, y'_{H_r} \mid y'_{H_r} = m_r x'_{H_r} + a_r\right\},$$

for some constants m_r and a_r. The values of m_r and a_r can be obtained easily by regressing a line on the image of the horizon. We know, therefore, that the projection matrix **P** associated with the camera must satisfy

$$(\mathbf{PX}_{H_i})_2 = m_r(\mathbf{P}_r\mathbf{X}_{H_i})_1 + a_r \ ,$$

where the $\mathbf{X}_{H_i}$ are elements of (6) and the subscripts 1 and 2 denote the first and second components of the image vector. This equation implicitly defines the camera's pitch and roll. When all other parameters are known, pitch and roll can be estimated by using a nonlinear optimization method (such as the Levenberg-Marquardt optimization[20]), with a cost function

$$C_h \ = \ \frac{1}{N_h}\sum_{i=1}^{N_h}\Big|m_r(\mathbf{P}_r\mathbf{X}_{H_i})_1 + a_r - (\mathbf{P}_r\mathbf{X}_{H_i})_2$$

3.2

The epipolar constraint

Let $\mathbf{X}'_l \ = \ \mathbf{P}_l\mathbf{X}$ and $\mathbf{X}'_r \ = \ \mathbf{P}_r\mathbf{X}$ be the projected pixel coordinates of some object at 3D world coordinate $\mathbf{X}$ onto right and left camera image planes, respectively. The epipolar line in the right camera's image plane is the image of all world coordinates that would project onto $\mathbf{X}'_l$ in the left camera's image plane. Likewise, the epipolar line in the left camera's image plane is the image of all world coordinates that would project onto $\mathbf{X}'_r$ in the right camera's image plane. If $\mathbf{P}_l$ and $\mathbf{P}_r$ are known perfectly, then $\mathbf{X}'_r$ will lie on the epipolar line in the right camera's image plane, and likewise for $\mathbf{X}'_l$ in the left camera's image plane. On the other hand, if $\mathbf{P}_l$ and $\mathbf{P}_r$ contain error, then images will not, in general, coincide with the epipolar lines. Note that changes in displacement, pitch, yaw, and roll that are applied equally to both cameras can not cause images to deviate from epipolar lines; only relative errors in these quantities manifest as deviations of images from epipolar lines.

This deviations of images from epipolar lines can be quantified using the "fundamental matrix" $\mathbf{F}$, which is constructed from $\mathbf{P}_l$ and $\mathbf{P}_r$.[16, 17] Note that, although $\mathbf{P}_l$ and $\mathbf{P}_r$ uniquely define the fundamental matrix, the reverse is not true. The fundamental matrix determines $\mathbf{P}_l$ and $\mathbf{P}_r$ up to an overall displacement, pitch, yaw, and roll; in other words, $\mathbf{F}$ gives the relative displacement, relative pitch, relative yaw, and relative roll of the left camera with respect to the right camera. If the calibration of $\mathbf{P}_l$ and $\mathbf{P}_r$ is perfect, then $\mathbf{X}'_l$ should lie on the epipolar line $\mathbf{l}_l = \mathbf{FX}'_r$. This can be formulated in terms of a cost function to estimate the relative pitch, relative yaw, and relative roll of the left camera with respect to the right camera through a nonlinear optimization method (such as the Levenberg-Marquardt optimization[20]), so that the distance from the pixel point $\mathbf{X}'_l$ to the epipolar line $\mathbf{FX}'_r$ is be minimized,

$$C_e = \frac{1}{N_e}\sum_{i=1}^{N_e}\frac{\left|\mathbf{X'}_{l_i}^{T}\mathbf{F}\mathbf{X'}_{r_i}\right|^2}{(\mathbf{F}\mathbf{X'}_{r_i})_1^2 + (\mathbf{F}\mathbf{X'}_{r_i})_2^2}.$$

3.3

Celestial Camera Calibration

Some of the brightest stars and planets which can be captured at night time images provide a very good source for camera calibration and has been used for this purpose for long baseline stereo applications.[14, 21]The angular position of stars at a given time with respect to a location on earth can be determined from various astronomy sources. We have used the java based JSkyCalc software[†] for this purpose. JSkyCalc provides the Greenwich Hour Angle (GHA) and Declination (DEC) of each star for a given time. GHA and DEC are the earthbound polar coordinates of the star, DEC being the northward angular distance and GHA being the eastward angular distance. The projection of a star at 3D coordinate $\mathbf{X}_s$ onto a camera image plane associated with a projection matrix $\mathbf{P}_s$ can be calculated as $\mathbf{P}_s\mathbf{X}_s$ and should be equal to the image of the star at pixel position $\mathbf{X'}_s$. The intrinsic camera parameters and Euler angle parameters (but not the translation parameters) of $\mathbf{P}_s$ can be solved through nonlinear optimization with a cost function based on the pixel distance between the identified pixel positions of the stars and the projected positions of the stars as

$$C_s = \frac{1}{N_s}\sum_{i=1}^{N_s}\left|\mathbf{X'}_s - \mathbf{P}_s\mathbf{X}_s\right|^2.$$

4.

AUTOMATIC CLOUD FEATURE DETECTION AND MATCHING

Our main aim is to collect measurements which will help us to understand the dynamics of developing convective clouds. Feature extraction in the scope of our work refers to identifying turret tops and boundaries and matching these pixels with their correspondences in the pairing stereo image. Assuming that the cameras are stereo calibrated, we can set the right camera as the reference and perform feature detection over the right image frame, and match the correspondences with the pairing left image frame by guidance of the epipolar lines. The cloud detection and matching algorithm can be summarized in three main steps as

- • detect and extract cloud regions in both image pair,
- • detect cloud features,
- • match the features at two -low and full resolution- passes.

The first step is a basic masking of cloud regions, in order to decrease the number of false identifications and to improve computation time. The cloud detection consists of thresholding in the blue channel scaled by the red channel to obtain a binary mask *M*,

$$M(i,j) = \begin{cases} 1, & \text{if } 0.84 < B(i,j)/R(i,j) < \\ 0, & \text{else} \end{cases}$$

where *B*(*i, j*) and *R*(*i, j*) denote the blue and red channel intensity values at (*i, j*)th pixel, respectively. Note that feature detection operates only over the masked region whereas matching operates over the unmasked image. In the second step, cloud features inside the masked region of the reference frame are detected. Cloud features are identified by a Canny edge detection. The third step is a two pass block matching algorithm working on two resolution scales. Let I_r, I'_r, I_l, and I'_l denote the grayscale intensities of full and low resolution right image frames, and full and low resolution left image frames, respectively. A pixel pair $(i'_l, j'_l) \in I'_l$ is said to match pixel pair $(i'_r, j'_r) \in I'_r$ if and only if the maximum correlation coefficient calculated in a search region of R_l,

$$c(i'_l, j'_l) = \max_{(i',j')\in R_l} \left\{ \frac{\sum_{m=-N_l}^{N_l} \sum_{n=-N_l}^{N_l} \left[I'_r(i'_r - m, j'_r \right.}{} \right.$$

exceeds a preset threshold, where

$$S = \sum_{m=-N_l}^{N_l} \sum_{n=-N_l}^{N_l} \left[I(i'-m, j'-n) - \bar{I}'(i',j') \right]$$

and $\bar{I}$ denotes averaging over $N_l \times N_l$ window. The search region R_l is limited by the disparity range in *i*′ and by the epipolar line in *j*′ directions. For each matched pair at the low resolution scale, a similar block matching algorithm is applied in order to obtain a higher resolution pixel pair match, such that $(i_l, j_l) \in I_l$ matches $(i_r, j_r) \in I_r$. Once high resolution pixel pair match is obtained, DLT[17] is used to reconstruct the 3D world coordinates.

5.

TEST RESULTS

In this section, test and validation results related to the calibration strategies introduced in Section 3 and the feature detection and matching algorithm presented in Section 4 are included. The cost functions presented in Section 3 can be combined together or used separately to solve for calibration parameters depending on the unknowns and available sources (night time images, horizon, corresponding points, etc.). We used the horizon and epipolar constraint together, $C_h + C_e$ to solve for the unknown parameters of Miami setting, after estimating absolute yaw of reference (right) camera from the position of Sun.[19] For SGP setting, we could locate eight bright stars and Jupiter at different positions on various days, and used $C_s + C_e$ to estimate absolute Euler angles of the left camera and relative Euler angles of the right camera with respect to the left camera.

5.1

Validating camera calibration

Validating the camera calibration is a challenge for our settings due to the difficulty in finding a ground truth data. In this work, we use wind speed measurements from radiosondes and cloud base measurements from ceilometer to validate the calibration parameters. Radiosondes are generally released at certain locations twice daily, at 24 UTC and 12 UTC, and the measurements are accessible publicly at the website of National Oceanic and Atmospheric Administration (NOAA)[‡]. The radiosonde release location for Miami (referred as MFL 72202 in NOAA database) is 10 km inland from the location of our cameras. Ceilometers in both Miami and SGP site are colocated with the cameras. Table 1 lists stereo reconstructed cloud base heights compared against ceilometer measurements for different days and cloud types at Miami and SGP settings. Ceilometer samples clouds with an upright laser beam. Hundreds of samples from a single frame can be obtained from the clouds in the field of view of the cameras, which can be as distant as tens of kilometers, whereas the ceilometer records one sample from the cloud right overhead in 15 seconds. Hence, we compare the statistics from a single frame against 20 min interval of ceilometer measurements. Samples of the Miami settings for the listed three frames are picked manually, whereas the samples from SGP frames are automatically detected.

Table 1.

Cloud-base statistics from the stereo cameras and ceilometers.

Date	timeUTC	# samplesstereo cam	av height(m)stereo cam	av height(m)ceilometer	std height(m)stereo cam	std height(m)ceilometer
Miami Setting						
April 8 2013	20:25	440	1804	1805	56	42
April 4	13:44	416	5904	5913	174	173

2013						
April 9 2013	11:20	307	11895	11512	690	159
SGP Setting						
April 21 2014	21:50	652	1798	1822	491	345
April 21 2014	21:50	652	3348	3295	138	60
May 14 2014	20:12	2025	2894	2969	180	93

Table 2 lists horizontal wind speeds estimated from reconstructed cloud altitudes compared against radiosonde measured (interpolated for the reconstructed cloud altitude) wind speeds. The reconstructed cloud altitudes and wind speeds agree with the radiosonde and ceilometer measurements as listed in Table 1 and Table 2. Stereo reconstructed altitudes display higher variance than the ceilometer measurements partly due to the fact that clouds as far as 39 km away are sampled by stereo images, and only overhead clouds are sampled by the ceilometer. Analysis of reconstruction error and impact of inaccuracies on calibration parameters are analyzed in detail in our previous work. [19] Reconstructed altitudes from SGP site possess even higher variance, mainly due to feature matching error.

Table 2.

Horizontal wind speeds calculated from reconstructed cloud altitudes and radiosonde measurements.

Date	time intervalUTC	av hght(m)	av u(m/s)	av v(m/s)	stdhght	stdu	std v	sonde u(m/s)	sonde v(m/s)
April 4	13:34 - 13:53	5916	-21.9	2.8	135	0.8	1.1	- 25.7	0
April 8	20:15 - 20:36	1817	-2.6	5.6	32	0.9	1.3	-2.8	4.9

April 9	11:11 - 11:34	741	5.9	-3.5	54	0.7	2.9	5.3	-3.1
April 9	11:10 - 11:24	11344	-35.0	1.7	522	2.1	2.4	-37.9	3.3

5.2

Estimating vertical motions in turret tops

Fig. 2 displays samples of turrets captured by Miami and SGP settings. Detection-matching-reconstruction is executed over image sequences of 30^{-1} s^{-1} frame rate. The turret tops are extracted from captured coordinates and are tracked in time. The vertical displacement of individual turret tops captured in Miami are displayed in **Fig. 3**. Estimated vertical velocities are displayed as the slopes of the fitted lines. The video file in **Video 1** displays a short movie of a developing convection that was captured in Miami, on August 2, 2013. Detected and matched turret top pixels inside a region of interest can be seen in the video. The bottom panel of the video displays instantaneous velocity, average velocity and maximum velocity that are estimated by using a second order polynomial fitting over the identified cloud tops. **Fig. 4** depicts both vertical and horizontal displacement of a convection cloud top captured at SGP site, in May 7, 2014. Radiosonde wind speed measurements[§] are also depicted at the rightmost panel for radiosonde release time 23:40 UTC. The radiosonde wind speed plot shows that eastward wind speeds change between 10 m/s to 24 m/s and northward wind speeds change between 10 m/s to 14 m/s from 5 km to 8 km altitude. This is consistent with the slopes of the horizontal cloud top displacements, 18 m/s in the eastward and 13 m/s in the northward direction.

Figure 2.

Active convections captured at Miami (top) and SGP (bottom) sites. Red numbers mark the automatically detected and matched positions in image pairs.

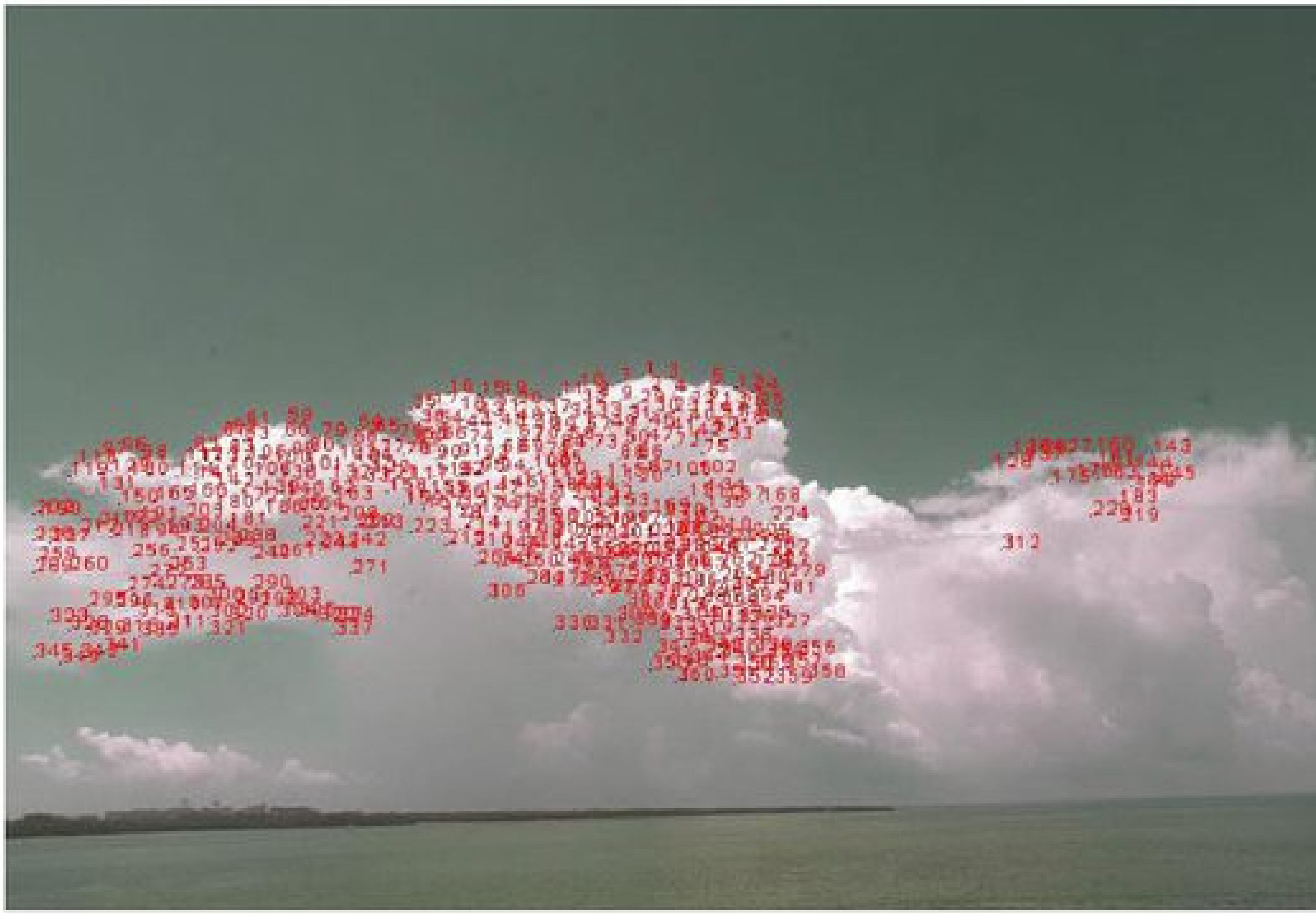

Figure 3.

Vertical displacements of individual turret tops captured in Miami.

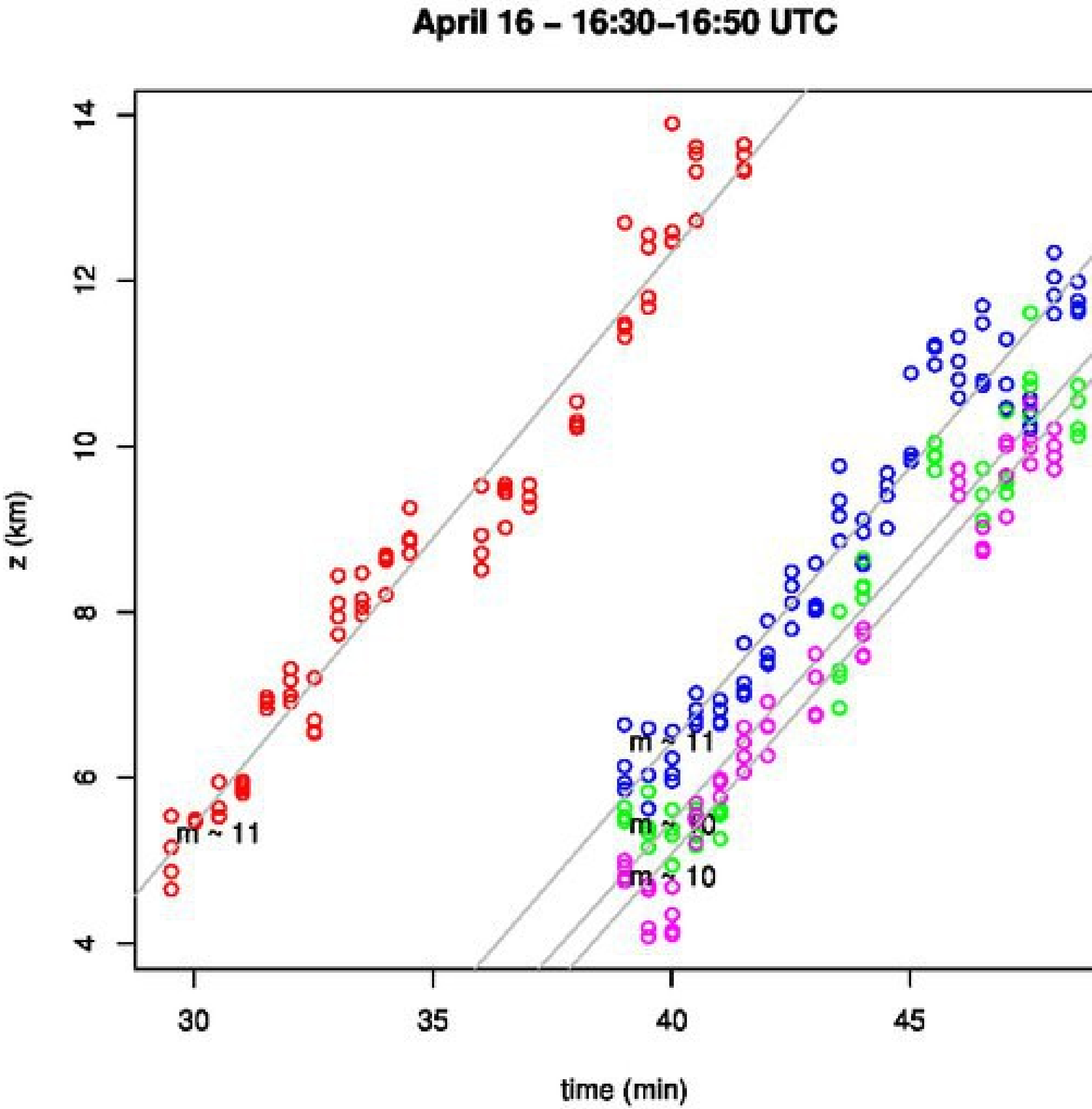

Video 1.

A short sequence of images displaying the automatically detected and reconstructed cloud top features. **http://dx.doi.org/10.1117/12.2083395.1**

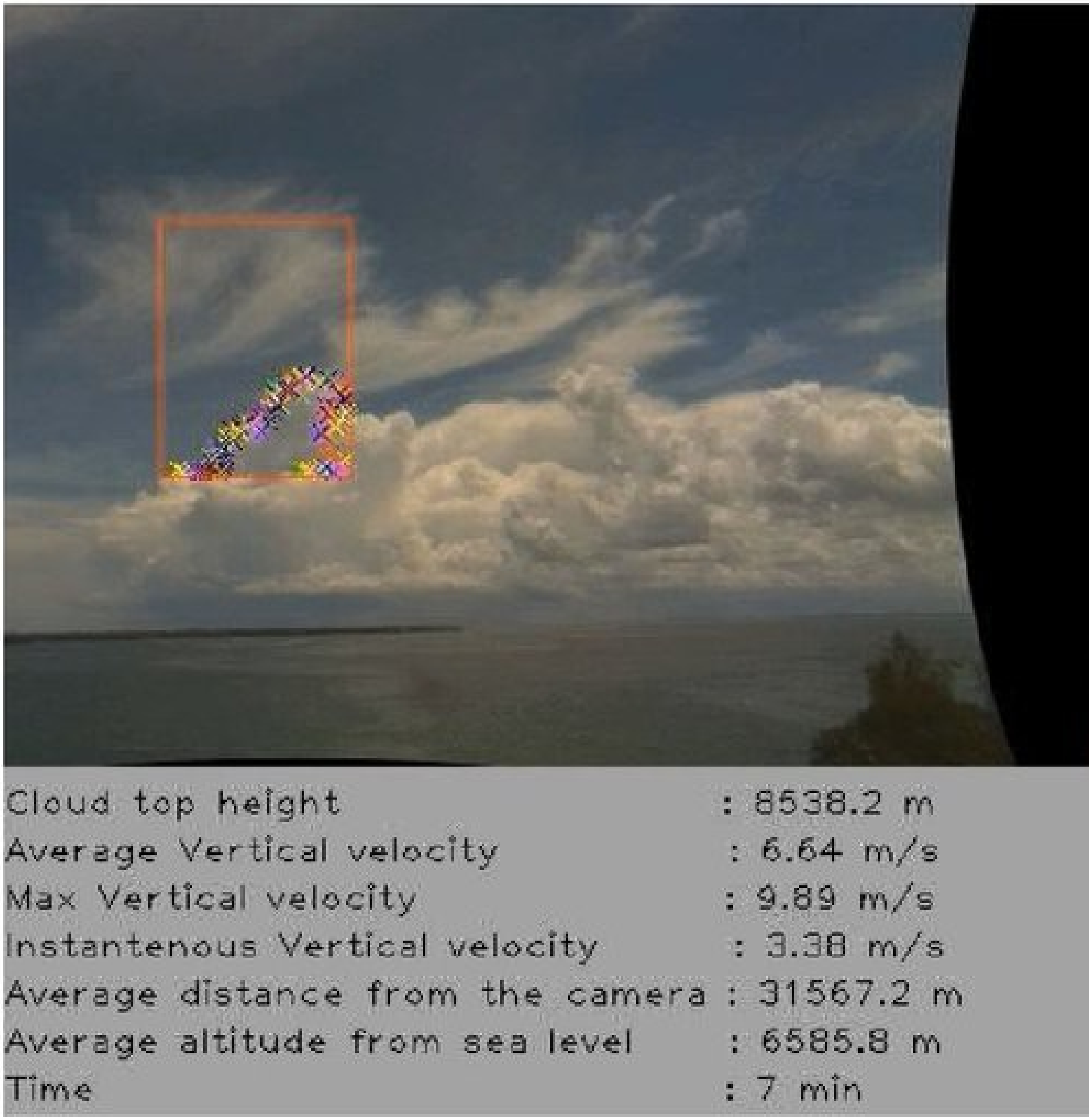

```
Cloud top height                     : 8538.2 m
Average Vertical velocity             : 6.64 m/s
Max Vertical velocity                : 9.89 m/s
Instantenous Vertical velocity        : 3.38 m/s
Average distance from the camera : 31567.2 m
Average altitude from sea level       : 6585.8 m
Time                                 : 7 min
```

Figure 4.

Vertical and horizontal displacement of a deep convection captured at SGP site, on May 7, 2015, starting from 20:25 UTC. From left to right, vertical displacement, northward displacement, eastward displacement, northward (red) and eastward (blue) radiosonde wind speeds.

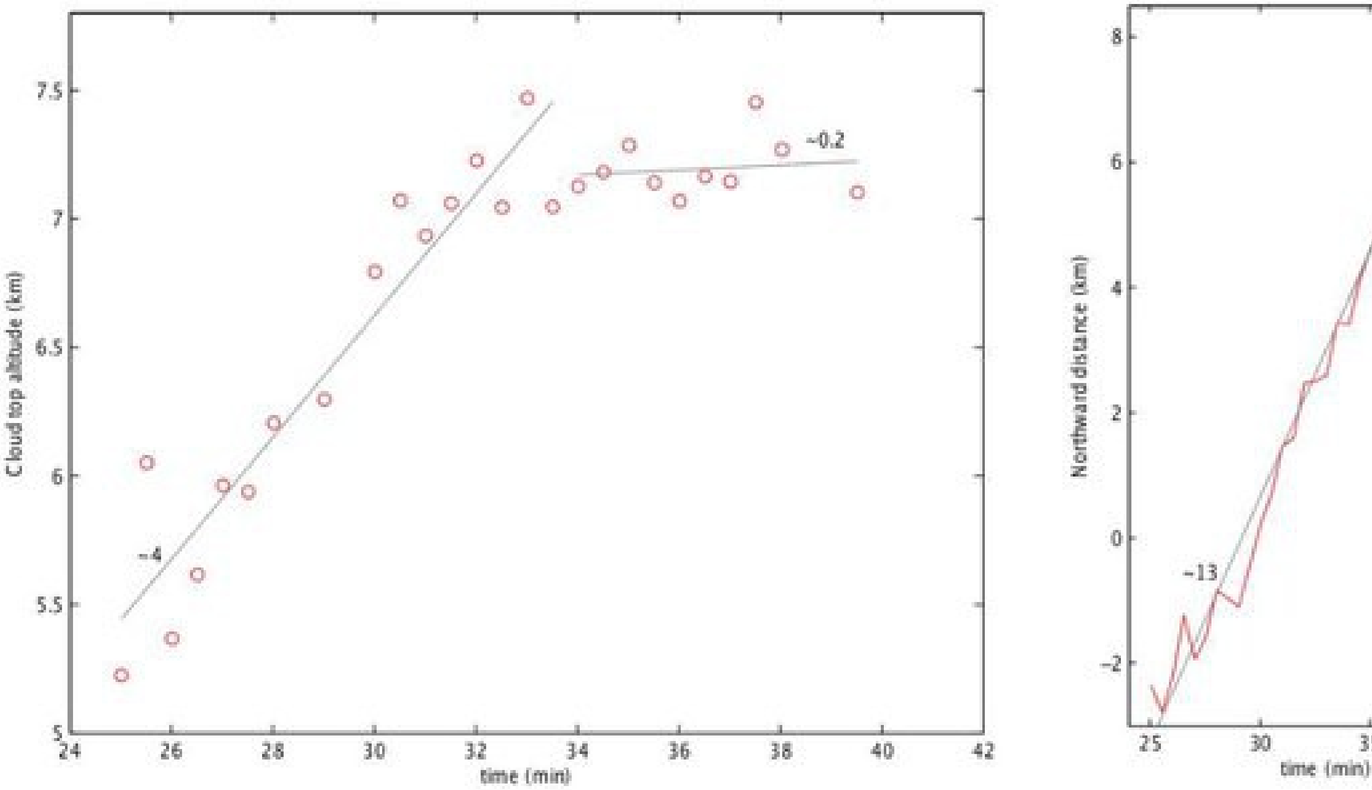

6. CONCLUSIONS

This paper describes the use of stereo photogrammetry and automatic feature detection and matching in atmospheric clouds observation. Stereo cameras have the capability to provide high resolution measurements on positions of clouds, which help to understand cloud dynamics. However outdoor stereo settings with a wide scene depth comes up with peculiar calibration challenges due to uncontrollable environment. Extrinsic camera calibration in outdoor settings is addressed in this work and different strategies are proposed. An automatic feature detection and stereo matching algorithm is introduced to track vertical motion of cloud tops over a sequence of images capturing developing convections. The introduced methods are tested and verified for two different outdoor stereo calibration settings. The reconstruction performance is validated against measurements obtained from meteorological instruments such as balloon radiosondes and ceilometer. The reconstructed cloud base heights and wind speeds show good agreement with the recorded measurements and proves the potential of stereo photogtrammetry in atmospheric cloud research.

Acknowledgments

This work was supported initially by the Laboratory Directed Research and Development Program of Lawrence Berkeley National Laboratory under U.S. Department of Energy Contract No. DE-AC02-05CH11231 and, subsequently, by the Hellman Fellows Fund. The Marine and Science Technology (MAST) Academy hosted one of the Miami cameras, and many thanks are due to the school administration and technical staff, without whom this project would not have been possible. The other Miami camera is owned by Rosenstiel School of Marine and Atmospheric Science (RSMAS), who shared their camera data with us.

REFERENCES

[1]
Mather, J. H. and Voyles, J. W., “The ARM climate research facility: A review of structure and capabilities,” Bulletin of the American Meteorological Society 94, 377–392 (Mar. 2013). **https://doi.org/10.1175/BAMS-D-11-00218.1**Google Scholar

[2]
Ackerman, T. P. and Stokes, G. M., “The atmospheric radiation measurement program,” Physics Today 56 (2003). **https://doi.org/10.1063/1.1554135**Google Scholar

[3]
Fielding, M. D., Chiu, J. C., Hogan, R. J., and Feingold, G., “3d cloud reconstructions: Evaluation of scanning radar scan strategy with a view to surface shortwave radiation closure,” Journal of Geophysical Research 118, 1–15 (Aug. 2013).Google Scholar

[4]
Kollias, P., Bharadwaj, N., Widener, K., Jo, I., and Johnson, K., “Scanning ARM cloud radars (SACR’s) Part I: Operational sampling strategies,” Journal of Atmospheric and Oceanic Technology (2014). **https://doi.org/10.1175/JTECH-D-13-00044.1**Google Scholar

[5]
Kassander, A. R. and Sims, L. L., “Cloud photogrammetry with ground-located K-17 aerial cameras,” Journal of Meteorology 14(1), 43–49 (1957). **https://doi.org/10.1175/0095-9634-14.1.43**Google Scholar

[6]
Orville, H. D. and Kassander, A. R., “Terrestrial photogrammetry of clouds,” Journal of Meteorology 18, 682–687 (Oct. 1961). **https://doi.org/10.1175/1520-0469(1961)018<0682:TPOC>2.0.CO;2**Google Scholar

[7]
Bradbury, D. L. and Fujita, T., “Computation of height and velocity of mesospheric clouds from dual, whole-sky, time-lapse picture sequences,” Satellite and Mesometeorology Research Project (SMRP) Paper No. 70, Department of Geophysical Sciences, University of Chicago, Chicago, Illinois (1968).Google Scholar

[8]
Warner, C., Renick, J., Balshaw, M., and Douglas, R., “Stereo photogrammetry of cumulonimbus clouds,” Quarterly Journal of the Royal Meteorological Society 99(419), 105–115 (1973). **https://doi.org/10.1002/(ISSN)1477-870X**Google Scholar

[9]
Allmen, M. C. and Kegelmeyer, P., “The computation of cloud-base height from paired whole-sky imaging cameras,” Journal of Atmospheric and Oceanic Technology 13(1), 97–113 (1996). **https://doi.org/10.1175/1520-0426(1996)013<0097:TCOCBH>2.0.CO;2**Google Scholar

[10]
Kassianov, E., Long, C. N., and Christy, J., “Cloud-base-height estimation from paired ground-based hemispherical observations,” Journal ofApplied Meteorology 44, 1221–1233 (Aug. 2005). **https://doi.org/10.1175/JAM2277.1**Google Scholar

[11]
Zehnder, J. A., Hu, J., and Razdan, A., “A stereo photogrammetric technique applied to orographic convection,” Monthly Weather Review 135(6), 2265–2277 (2007). **https://doi.org/10.1175/MWR3401.1**Google Scholar

[12]
Damiani, R., Geerts, B., Demko, J., Haimov, S., French, J., Zehnder, J., Razdan, A., Hu, J., Petti, J., Leuthold, M., and Poulos, G. S., “The Cumulus, Photogrammetric, In Situ, and Doppler Observations experiment of 2006,” Bulletin of the American Meteorological Society 89(1), 57–73 (2008). **https://doi.org/10.1175/BAMS-89-1-57**Google Scholar

[13]
Zehnder, J., Zhang, L., Hansford, D., Radzan, A., Selover, N., and Brown, C., “Using digital cloud pho-togrammetry to characterize the onset and transition from shallow to deep convection over orography,” Monthly Weather Review 134(9), 2527–2546 (2006). **https://doi.org/10.1175/MWR3194.1**Google Scholar

[14]
Seiz, G., Baltsavias, E. P., and Gruen, A., “Cloud mapping from the ground: Use of photogrammetric methods,” Photogrammetric Engineering & Remote Sensing 68(9), 941–951 (2002).Google Scholar

[15]
Hu, J., Razdan, A., and Zehnder, J. A., “Geometric calibration of digital cameras for 3d cumulus cloud measurements,” Journal of Atmospheric and Oceanic Technology 26(2), 200–214 (2009). **https://doi.org/10.1175/2008JTECHA1079.1**Google Scholar

[16]
Forsyth, D. A. and Ponce, J., [Computer Vision: A Modern Approach], Prentice Hall (2003).Google Scholar

[17]
Hartley, R. and Zisserman, A., [Multiple view geometry in computer vision], Cambridge University Press (2003).Google Scholar

[18]
Bradski, G. and Kaehler, A., [Learning OpenCV, Computer Vision with the OpenCV Library], O’Reilly (2008).Google Scholar

[19]
Oktem, R., Prabhat, Lee, J., Thomas, A., Zuidema, P., and Romps, D. M., “Stereo photogrammetry of oceanic clouds,” Journal of atmospheric and Oceanic Technology 31(7), 1482–1501 (2014). **https://doi.org/10.1175/JTECH-D-13-00224.1**Google Scholar

[20]
Press, W. H., Teukolsky, S. A., Vetterling, W. T., and Flannery, B. P., [Numerical Recipes: The Art of Scientific Computing], Cambridge University (2007).Google Scholar

[21]

Danescu, R., Oniga, F., Turcu, V., and Cristea, O., “Long baseline stereovision for automatic detection and ranging of moving objects in the night sky,” Sensors 12, 12940–12963 (2012). **https://doi.org/10.3390/s121012940**Google Scholar

Notes

[1] **http://carob.rsmas.miami.edu**

[2] **http://www.dartmouth.edu/~physics/labs/skycalc/flyer.html**

[3] **http://www.esrl.noaa.gov/raobs**

[4] **http://www.arm.gov/instruments/sonde**